The Astrophysical Journal, 970:35 (9pp), 2024 July 20 https://doi.org/10.3847/1538-4357/ad50c9

Quantitative Comparisons between WSA Implementations

Shaela I. Jones[1,2], Ronald M. Caplan[3], C. Nick Arge[1], Jon A. Linker[3], Carl J. Henney[4], Raphael Attie[1,2],
Cooper Downs[3], Bibhuti Kumar Jha[5], James Turtle[3], and Lisa Upton[5]
[1] NASA Goddard Space Flight Center, Code 670, Greenbelt, MD 20771, USA; shaela.i.jonesmecholsky@nasa.gov
[2] Catholic University of America, 620 Michigan Avenue, N.E. Washington, DC 20064, USA
[3] Predictive Science Inc., 9990 Mesa Rim Road Suite 170, San Diego, CA 92121, USA
[4] Air Force Research Laboratory, Space Vehicles Directorate, Kirtland AFB, NM 87117, USA
[5] Southwest Research Institute, Boulder, CO 80302, USA

Received 2023 November 28; revised 2024 May 17; accepted 2024 May 25; published 2024 July 15

Abstract

The Wang–Sheeley–Arge (WSA) model has been in use for decades and remains a popular, economical approach to modeling the solar coronal magnetic field and forecasting conditions in the inner heliosphere. Given its usefulness, it is unsurprising that a number of WSA implementations have been developed by various groups with different computational approaches. While the WSA magnetic field model has traditionally been calculated using a spherical harmonic expansion of the solar magnetic field, finite-difference potential field solutions can offer speed and/or accuracy advantages. However, the creation of new versions of WSA requires that we ensure the solutions from these new models are consistent with established versions and that we quantify for the user community to what degree and in what ways they differ. In this paper, we present side-by-side comparisons of WSA models produced using the traditional, spherical harmonic–based implementation developed by Wang, Sheeley, and Arge with WSA models produced using a recently open-sourced finite-difference code from the CORHEL modeling suite called POT3D. We present comparisons of the terminal solar wind speed and magnetic field at the outer boundaries of the models, weighing these against the variation of the WSA model in the presence of small perturbations in the computational procedure, parameters, and inputs. We also compare the footpoints of magnetic field lines traced from the outer boundaries and the locations of open field in the models. We find that the traced field-line footpoints show remarkable agreement, with the greatest differences near the magnetic neutral line and in the polar regions.

Unified Astronomy Thesaurus concepts: Solar corona (1483); Solar coronal lines (2038); Space weather (2037); Solar wind (1534); Interplanetary magnetic fields (824); Model selection (1912)

1. Introduction

Predicting solar wind and interplanetary magnetic field (IMF) conditions is important for understanding the physical evolution and propagation of coronal mass ejections and solar energetic particles and forecasting space-weather conditions. The WSA model (Arge & Pizzo 2000; Arge et al. 2003) is a semi-empirical model for the coronal magnetic field and solar wind speed and IMF polarity in the inner heliosphere and has been in popular use for decades (Sheeley 2017). The model consists of two potential magnetic field–type models residing in two concentric spherical shells. The inner shell holds a Potential Field Source Surface (PFSS) model, extending from the photosphere to a fixed radius called the source surface, R_{ss}. The outer shell extends from an interface radius R_{int} to the outer boundary of the model (often taken to be either 0.1 au or 5.0 $R_\odot$, depending on the application). The Schatten current sheet (SCS) model (Altschuler & Newkirk 1969; Schatten et al. 1969) is used to determine the magnetic field solution in this outer shell. In the SCS shell, the sign of the magnetic flux is taken to be positive everywhere on the inner boundary, and the magnetic field is solved as in the PFSS model. This forces all field lines that reach the inner boundary to be open and results in more even flux distribution at the outer boundary and elongated streamer structures similar to those seen in images of the corona but at the cost of an unphysical discontinuity at the inner boundary. The sign of the field at a given point can be determined by tracing the magnetic field down to R_{int}. In most versions of this combined model (e.g., Wang & Sheeley 1995), the interface radius and source-surface radius are set to the same value, where the radial magnetic field at the source surface serves as the inner boundary to the SCS. In WSA, a small overlap region between the source surface and interface radius is used to connect the two models with default radii of 2.51 $R_\odot$ and 2.49 $R_\odot$, respectively.

In addition to the coronal magnetic field, the WSA model provides an estimate of the terminal solar wind speed at the model outer boundary given by

$$V = V_0 + \frac{V_m}{(1 + f_{exp})^{C_1}}\left(1 - C_2 \exp\left[-\left(\frac{\Theta_B}{C_3}\right)^{C_4}\right]\right)^{C_5}, \quad (1)$$

where V_0, V_m, and C_1–C_5 are empirically determined parameters. The magnetic field flux tube expansion factor, f_{exp}, is a measure of the expansion of the local magnetic field between the photosphere and R_{ss}. It is calculated as described in Wang & Sheeley (1990), $f_{exp} = (R_\odot/R_{ss})^2(B(R_\odot)/B(R_{ss}))$, where $B(R_\odot)$ and $B(R_{ss})$ are the magnetic field strength at the photosphere and the source surface for a given magnetic field line traced through the WSA model. Θ_B is referred to as the coronal hole boundary distance (the minimum angular

Table 1
Parameter Values Used for Solar Wind Speed Predictions in Equation (1)

V_0 (m s^{-1})	V_m (m s^{-1})	C_1	C_2	C_3	C_4	C_5
286	625	2/9	0.8	1	2	3

separation between the photospheric footpoints of the local magnetic field line and the nearest open-field region; Arge & Pizzo 2000; Arge et al. 2004; Wallace et al. 2020; Wang & Sheeley 1990; Levine et al. 1977).[6]

The parameters in Equation (1) have changed over time (see McGregor et al. 2011 and references therein); therefore, it is very important that authors specify the code, version number, and parameter values used when publishing results of a WSA model. The values used in this paper are those currently in use by the Arge et al. team at the NASA Goddard Space Flight Center, in version 5.4.0 of their code (Wang et al. 2022), and are given in Table 1.[7]

The terminal solar wind speed and magnetic field at the outer boundary of the coronal portion of the WSA model are frequently used as inner boundary conditions for magnetohydrodynamic (Odstrcil et al. 2005; Pahud et al. 2012; Kim et al. 2020) models of the heliosphere. Alternatively, the IMF polarity and solar wind speed can be forecasted at a point of interest in the inner heliosphere by making use of the 1D kinematic solar wind code within WSA, which propagates hypothetical solar wind macroparticles quasiballistically through the heliosphere (Arge & Pizzo 2000). In this code, stream interactions are accounted for, in a very simple ad hoc manner.

Traditionally, the global coronal magnetic field in WSA is determined using a spherical harmonic series solution to Laplace’s equation. This approach is used for the both the PFSS and SCS solutions within WSA. However, with increases in computational capability in recent decades, finite-difference methods have come to represent a viable (and sometimes preferable) alternative (Tóth et al. 2011). One such implementation is in the Corona-Heliosphere (CORHEL) model suite (Linker et al. 2009) and is of particular interest because the PFSS magnetic field solver was recently released as the open-source POT3D code (Caplan et al. 2021a). This code was described in Caplan et al. (2021b), where the authors validated the second-order convergence on a known analytic solution and demonstrated the variability to be expected from PFSS solutions given different photospheric map sources, source-surface radii, and model resolutions.

POT3D’s speed and scalability offer significant advantages over traditional, spherical harmonic–based solution schemes, including generating solutions at much higher resolutions, which will be the subject of future work. However, before attempting such higher-resolution problems, it is important to verify that the solutions at standard resolution match traditional results. In this paper, we make a comprehensive comparison of WSA coronal magnetic field models and solar wind predictions produced using CORHEL’s implementation (hereafter WSA-POT3D) with those produced using the Arge et al. code, version 5.4.0 (hereafter WSA-SH, for WSA-spherical-harmonic; Wang et al. 2022).

2. Making an Apples-to-apples Comparison

The WSA model calculation begins with a global map of the photospheric magnetic field distribution, which serves as its primary input. Here we have used photospheric maps created using the Air Force Data Assimilative Photospheric Flux Transport (ADAPT) model (Arge et al. 2010, 2013; Hickmann et al. 2015; Barnes et al. 2022; Schonfeld et al. 2022), based on Solar Dynamics Observatory Helioseismic and Magnetic Imager (HMI) line-of-sight magnetic flux measurements (Schou et al. 2012). ADAPT assimilates the remapped Br estimates into the modeled global photospheric map, which is updated using surface flux transport processes. The inferred full-disk line-of-sight magnetograms are remapped into heliographic coordinates, and the radial component Br is estimated using the radial field assumption, that is, by dividing the observed values by μ (cosine of the angle between the pixel and disk center). While the differential rotation and meridional flow are fairly regular, the turbulent photospheric supergranulation has substantial variation, which can have a significant impact on the flux distribution, especially at the poles. To account for supergranulation, ADAPT generates an ensemble of 12 members (or realizations) based on different random flow patterns resulting in different transport path histories for flux elements. With each realization representing a different and equally valid configuration of previously observed values, the ensemble collectively represents, at least in principle, the uncertainty in global photospheric magnetic field distribution. Using the ADAPT maps for our tests allows us to estimate the relative importance of model differences in light of our uncertainty about the photospheric boundary condition.

Figure 1 shows the synoptic map used for the model comparisons in this paper and the difference between this map and $B_r\,(r = 1.0\ R_\odot)$ in the WSA-SH model.

Even given the same input map, two WSA model codes will produce slightly different results. The WSA-SH and WSA-POT3D models both trace field lines from the outer boundary to the photosphere in order to determine the field polarity, expansion factor f_{exp}, and coronal hole boundary distance Θ_B on a grid at the outer boundary of the model, but the WSA-SH code includes an adjustable region of overlap between the inner and outer shells where the tracing is interrupted (Meadors et al. 2020). Both models also perform field-line tracing outward from the inner boundary of the model to ensure all coronal hole boundaries are correctly identified prior to calculating Θ_B, but the WSA-SH code starts from slightly above the photosphere to minimize the impact of ringing in the spherical harmonic transform. And, while WSA-POT3D’s field-line tracer uses an adaptive tracing step size with a second-order predictor-corrector scheme, WSA-SH makes use of the adaptive step Runge–Kutta–Fehlberg (RKF) method (Mathews & Fink 2004) for tracing magnetic field lines, where fifth- and fourth-order Runge–Kutta solutions are compared, and then the field-line tracing step size is adjusted to maintain a specified accuracy. Finally, the WSA-SH and WSA-POT3D models are computed on different grids—the WSA-SH model grid is evenly spaced

---

[6] The term “coronal hole” has sometimes been used interchangeably with “open-field region” to refer to regions of the magnetic field model where the photosphere is magnetically connected to the outer boundary, reflecting the common belief that coronal holes observed in coronagraph images likely result from mass streaming away from the corona along such field lines. Here we primarily use open-field region but maintain the term coronal hole boundary distance for Θ_B to be consistent with historical usage.

[7] C_3 is resolution dependent. The value used here is for 1° model runs.

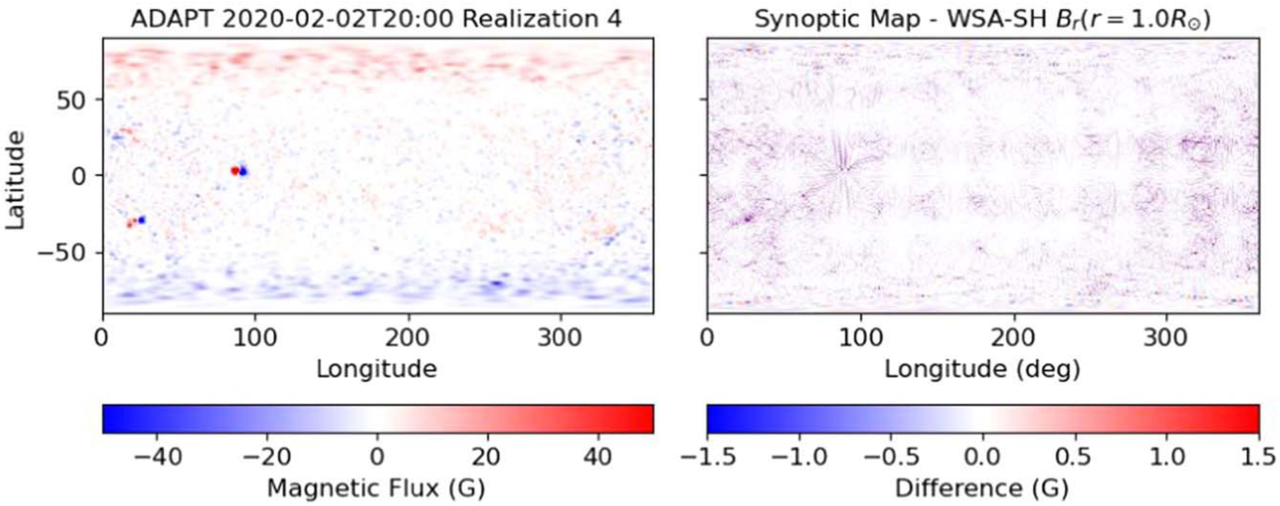

Figure 1. This figure illustrates (left) the ADAPT photospheric synoptic map used for our model comparison and (right) the difference between the photospheric map and the calculated B_r at the photosphere in the WSA-SH model. The ADAPT map dynamic range has been limited to ±50G to increase the visibility of magnetic structure in the lower flux range. The largest differences in the right panel are concentrated near the active regions, and the greatest difference is 4.54G.

in latitude/longitude, with the edges of the grid cells lying exactly on the polar and periodic boundaries, while the WSA-POT3D grid is not evenly spaced in latitude/longitude, and the grid cells are centered such that the boundary cell edges extend past the domain boundaries by half a cell (resulting in a one-cell overlap in the periodic ϕ direction and two rows of redundant values for each θ polar boundary).

Since our goal was to make comparisons between WSA-SH and WSA-POT3D models calculated as similarly as possible, we took special care to minimize the differences described above. We have chosen an ADAPT input map with minimal net magnetic flux so that both models could be computed without their respective flux balancing. Both models were computed at the resolution of the input maps (1°) with no smoothing or binning. The WSA-SH model was altered to trace from 1.00 $R_\odot$ like WSA-POT3D, while the WSA-POT3D model was altered to trace field lines for the computation of $f_{\rm exp}$ and Θ_B on the same grid cells as WSA-SH and perform the magnetic field computation on a grid with uniform latitudinal resolution.

3. Results

Figure 2 shows a comparison between the WSA-SH and WSA-POT3D models at their outer boundaries (located at $R = 21.5\ R_\odot$) based on the fifth realization of an ADAPT-HMI photospheric magnetic field map from 2020 February 2, 20:00 (Henney 2020). (This time period was difficult to model, coinciding with a fairly extreme solar-B angle and an extremely flat, solar minimum current sheet. None of the WSA models for this time period produce great solar wind forecasts, but the fifth realization was judged the best of the available options, based on comparisons between forecast and observed solar wind and IMF polarity at the Advanced Composition Explorer spacecraft. We use it here to measure the similarity of the two models, without regard to forecast accuracy.) The left panels compare the radial magnetic field, and the right panels compare the predicted terminal solar wind speed at the outer boundary of the WSA-SH (top) and WSA-POT3D (middle) models. The bottom panels show the absolute difference between the two model versions.

3.1. Magnetic Field Differences

The lower left-hand panel of Figure 1 shows the absolute difference in radial magnetic field between the two model solutions. It is dominated by a thin, scattered strip of pixels near the magnetic neutral line. This feature arises due to the differences in the field-line tracing methodologies used in the two models, which, when close to the current sheet, can cause one model to connect to the north pole while the other connects to the south. Since the magnitude of the magnetic fields are very similar in the two solutions, the apparently large discrepancies in the solutions reflect mainly differences in the field-line tracing and not the magnetic field solution itself. At 1° resolution, only about 0.08% of outer boundary pixels have opposite polarity. Away from the current sheet, there is a noticeable structure to the difference between the two magnetic field slices, with a narrow band of near-zero difference at low latitudes in each hemisphere, and gradually increasing differences toward the poles and the equator. These structural differences are not due to differences in the computational grids of the two codes as they are unaffected by adjustments to the grid spacing. However, the magnitude of the differences is very small, approximately only 1% of the typical field strength.

3.2. Terminal Wind Speed Differences

The terminal solar wind speed values seen in the top two panels in the right column of Figure 2 are very similar over most of the outer boundary, with differences concentrated in the vicinity of the magnetic neutral line and some more diffuse, smudgy regions at low- and midlatitudes.

To understand the sources of predicted wind speed differences between the two models, we examined the photospheric footpoints of the magnetic field lines from which $f_{\rm exp}$ and Θ_B are calculated. Starting at each grid cell center on the outer boundary, the field was traced down to the photosphere using the WSA-SH and WSA-POT3D models. The expansion factor was calculated for each field line traced by each model, and the footpoint latitudinal and longitudinal positions were recorded.[8]

---

[8] The expansion factor was calculated using the magnetic fields at 1.0 $R_\odot$ and 2.500 $R_\odot$ (2.501 $R_\odot$) for the WSA-POT3D (WSA-SH) model.

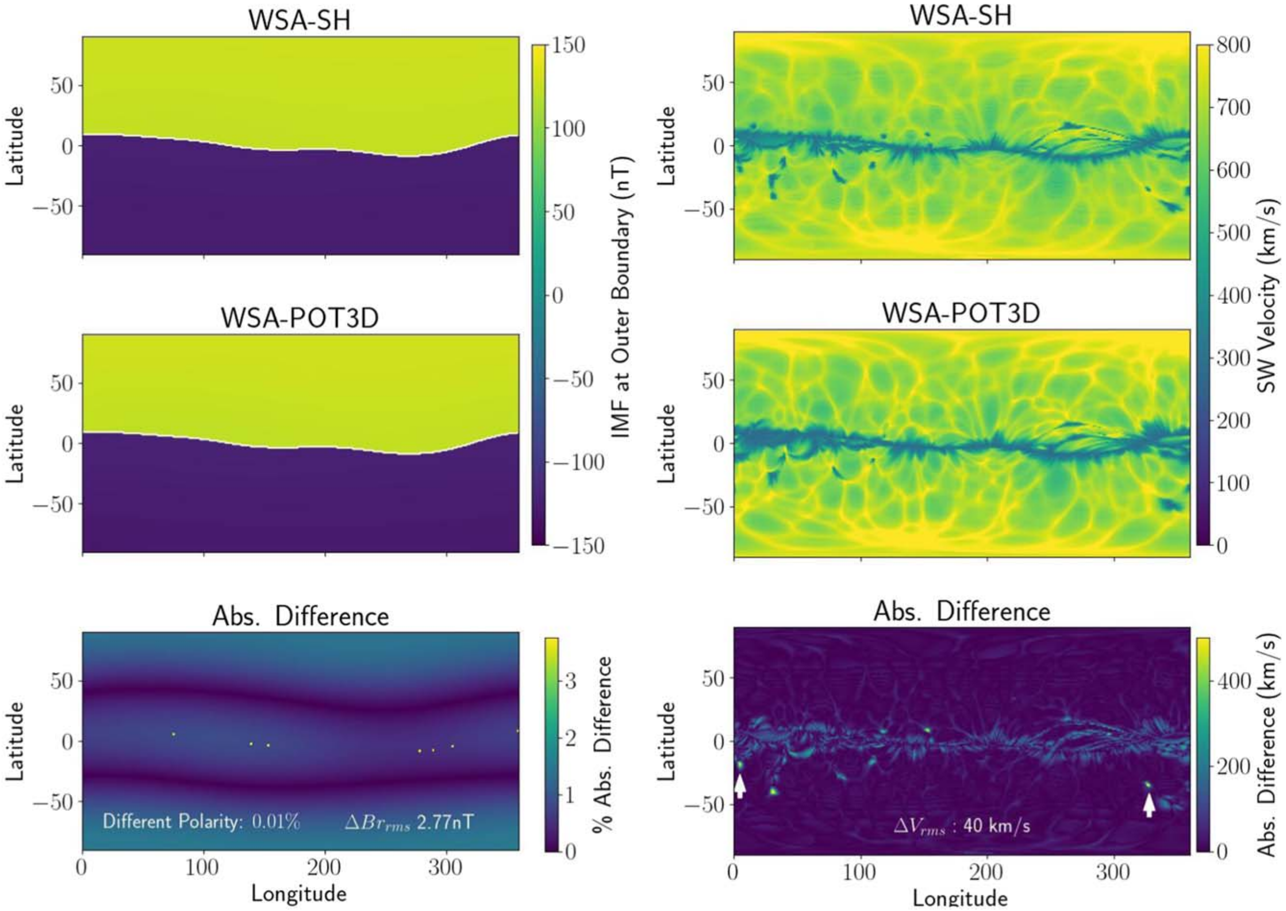

Figure 2. Comparison between WSA-SH model outer boundaries for 2020 February 2, 20:00. The left column shows the magnetic fields, and the right column shows the model-derived terminal solar wind speed. The top and middle panels are calculated using the WSA-SH and WSA-POT3D models, respectively. The bottom panel shows the absolute difference between the results of the two codes.

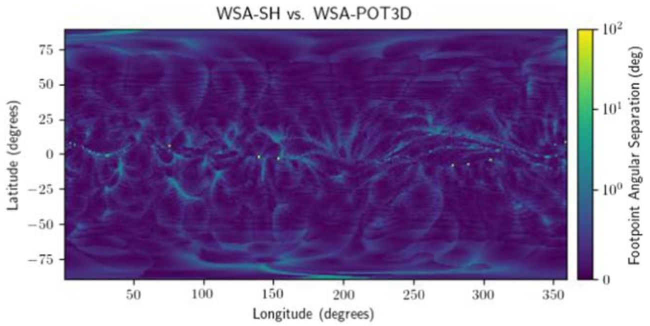

Figure 3. Angular separation between WSA-SH and WSA-POT3D model field-line footpoints at the photosphere as a function of starting position on the model outer boundary.

The absolute difference in expansion factor and footpoint position were calculated for equivalent field lines from the two models. Figure 3 shows the angular separation (in degrees) between corresponding footpoints of the WSA-SH and WSA-POT3D models, where the values are plotted on the outer boundary of the model (i.e., where the inward tracing of the field lines began). As expected, the greatest angular footpoint differences occur for field lines traced near the magnetic neutral line, with other areas of significant difference concentrated near the poles and along narrow, line-like features tracing out apparent magnetic separatrices.

Comparing Figure 3 with the bottom right panel of Figure 2, the large velocity differences seen between the two models do not seem to coincide with large separations between the model footpoints. Figure 4 shows the partial derivatives of Equation (1) with respect to the two model-based variables, $f_{\rm exp}$ and Θ_B in the WSA-SH model, as calculated by taking the partial derivatives of Equation (1) analytically:

$$\frac{\partial V}{\partial \Theta_B} = \left(\frac{C_2 C_4 C_5}{C_3}\right)\left(\frac{\Theta_B}{C_3}\right)^{(C_4-1)} \times \left(\exp\left[-\left(\frac{\Theta_B}{C_3}\right)^{C_4}\right] - C_2\right)(V - V_0), \tag{2}$$

$$\frac{\partial V}{\partial f_{\rm exp}} = \frac{-C_1}{1 + f_{\rm exp}}(V - V_0). \tag{3}$$

Close inspection reveals that there is almost a one-to-one correspondence between large differences in solar wind speed predictions between the two models and large values of $\partial V / \partial \Theta_B$ (evaluated using the WSA-SH solution for V). There seems to be little correlation between the large speed differences between the two models and $\partial V / \partial f_{\rm exp}$, suggesting that even big differences in $f_{\rm exp}$ play a small role in producing this effect. Figure 5 is a plot of Equation (1) as a function of Θ_B for five different fixed values of $f_{\rm exp}$. As can be seen in the figure, the predicted solar wind speed changes rapidly over a

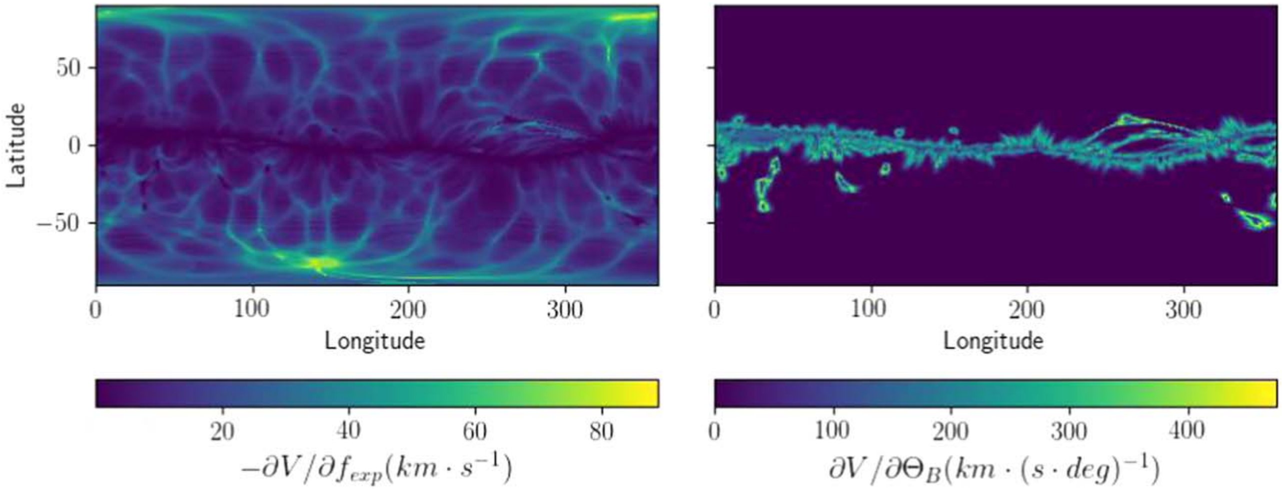

Figure 4. Partial derivative of the predicted terminal solar wind speed for 2020 February 2, 20:00 at the outer boundary of the WSA model, with respect to (left) expansion factor (f_{exp}) and (right) coronal hole boundary distance (Θ_B), using Equation (1) with the parameters specified in Table 1. The two variables appear to dominate the predicted wind speed in distinct spatial regions. The strongest differences between the WSA-POT3D and WSA-SH predicted speeds seen in Figure 2 correspond well to regions of high sensitivity. The Θ_B sensitivity tends to be highest near the magnetic neutral line, while f_{exp} sensitivity is higher away from this region. The relative importance of Θ_B and f_{exp} in the prediction of solar wind speeds is thus dependent on location in the heliosphere.

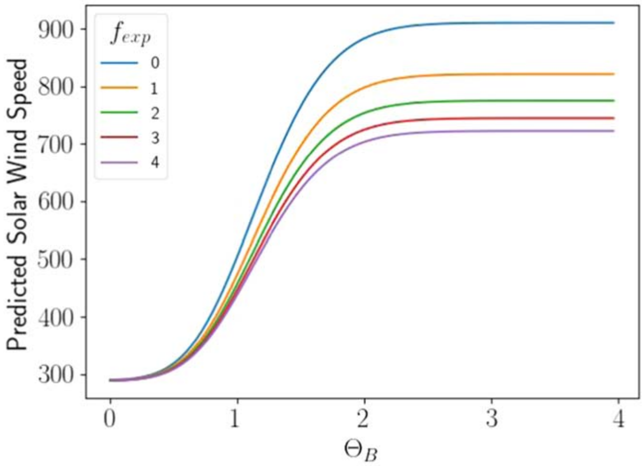

Figure 5. WSA empirical solar wind speed as a function of Θ_B for several fixed values of f_{exp}. Note how small changes in Θ_B can produce large changes in velocity for values of between 0°.5 and 1°.5 but make little difference outside this narrow, rapidly changing transition region.

narrow 1° range in Θ_B spanning from about 0°.5–1°.5 in coronal hole boundary distance. The value of f_{exp} appears to play a minimal role in this interval. It is evident that the large differences between the velocities of the two models corresponds to the region where Equation (1) is rapidly changing over a narrow range in Θ_B. It demonstrates that relatively small differences between the two models footpoints can have a significant impact on the predicted speeds if the values of Θ_B reside in this narrow band. Outside this region (e.g., deep inside an open-flux region), even large differences in Θ_B between the two models have minimal impact on the predicted speeds.

While the sensitivity maps in Figure 4 help explain the thin lines of higher velocity difference in the bottom right panel of Figure 2, they do not explain some of the less structured, smudge-like regions of model disagreement at low- to midlatitudes (see examples indicated with white arrows in Figure 2). Most of these regions have comparatively low speed in the WSA-SH model. The reason for these differences can be seen in Figure 6, which shows the locations of open-field regions within the two models. Both models show regions of closed magnetic flux embedded in the otherwise open-field regions, particularly near the south pole. However, the WSA-SH model has more of them, many quite small (see examples indicated by black arrows), and the larger of these parasitic closed-flux regions have somewhat more jagged edges than in the WSA-POT3D model.

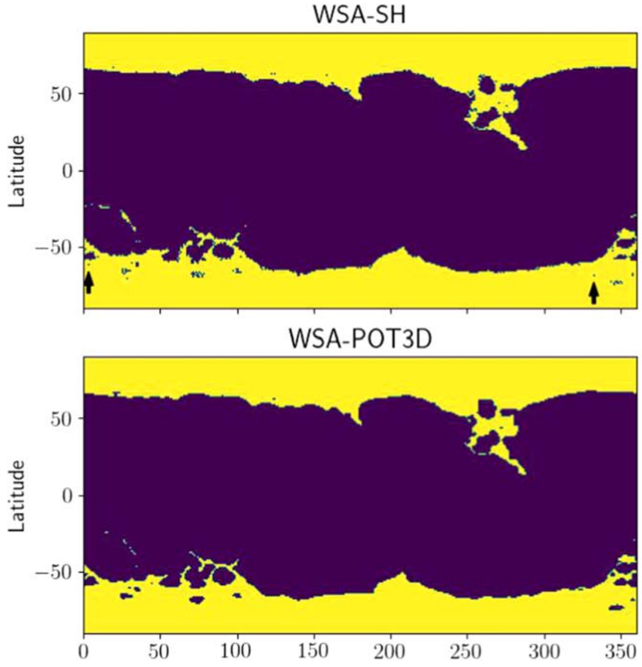

Figure 6. Open-field maps for 2020 February 2, 20:00, from the WSA-SH and WSA-POT3D models compared in Figure 2. Regions of open magnetic field are shown in yellow, with closed-field regions shown in purple.

The result of each of these parasitic closed-flux regions is a diffuse region of depressed solar wind speed at the outer boundary because the edges of these regions are considered part of the open-field boundary for the purposes of calculating Θ_B for Equation (1). This is the source of the patchy areas of

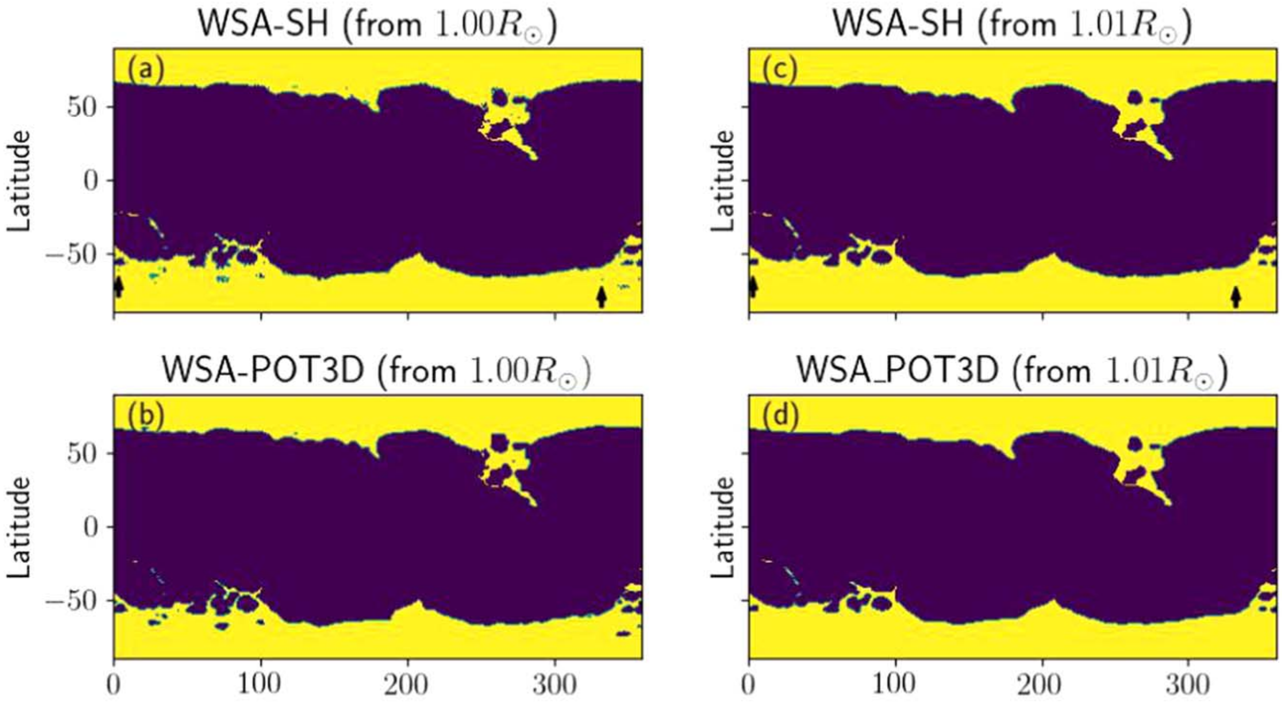

Figure 7. Open-flux maps for 2020 February 2, 20:00. Panels (a) and (b) show the open flux from the WSA-SH and WSA-POT3D models as in Figure 6, whose panels (c) and (d) show the same models but with the open flux determined by tracing the magnetic field from 1.01 $R_\odot$ rather than the photosphere. Tracing from the higher height has removed some parasitic closed-flux regions from the southern polar coronal hole.

low wind speed predictions in the southern midlatitudes in Figure 2. The WSA-SH model, seen in the top panel, has more of these low-speed patches because it has more parasitic closed-flux regions.

Why does the WSA-SH model have more parasitic closed-flux regions? These parasitic closed-flux regions within the polar open-field regions are precisely the reason why upward-traced field lines in the WSA-SH model are usually traced starting from 1.01 $R_\odot$. The spherical harmonic approximation of the photospheric flux map used in the WSA-SH model may sometimes have a sign opposite to that of the original map if the original flux value was very low. In open-field regions, this can result in an artificial, low-lying, closed-flux feature embedded within the open-field region. Most of these artificial closed-field regions close below 1.01 $R_\odot$, so tracing from this height avoids counting them as part of the open-field boundary.

In Figure 7, we show the open-flux locations in the WSA-SH and WSA-POT3D models, with field lines traced from 1.00 $R_\odot$ as in Figure 6 and from 1.01 $R_\odot$. While we can see that tracing from the higher height has eliminated the artificial closed-flux regions from the WSA-SH model, it has also removed some legitimate closed-flux regions that were found in both models. Panels (a) through (c) in Figure 8 show a velocity prediction comparison similar to the one in Figure 2 but based on the WSA-SH model with field lines traced from 1.01 $R_\odot$. The removal of the parasitic closed-flux regions has removed several of the patchy low-speed regions that appeared only in the WSA-SH model. However, it has also removed some low-speed regions that now appear only in the WSA-POT3D map (e.g., the large patch near 340° longitude, −45° latitude). Tracing the WSA-POT3D models from 1.01 $R_\odot$ (see Figure 8 panels (d) through (f)) eliminates these differences though that is likely undesirable as these are associated with legitimate closed-flux regions in the southern polar coronal hole that close below 1.01 $R_\odot$. This may indicate that using 1.01 $R_\odot$ as the starting height for upward field-line tracing in the WSA-SH model is too high. Unfortunately, the determination of an ideal starting height for the field-line tracing is beyond the scope of this paper. Furthermore, the ideal value most likely varies from map to map as well as depends upon the number of spherical harmonics used.

4. Comparisons with Internal Model Variability

Based on the analysis above, most of the differences between the WSA-SH and WSA-POT3D models are explainable, but are they significant? For comparison, we decided to measure the variability of the WSA-SH code with slight variations in the model inputs and parameter values. To measure the model internal variability, we generated the WSA-SH model solution under typical run conditions and compared it with alternative solutions where the model inputs and parameters were changed in the following ways:

1. Using different ADAPT ensemble members as input.
2. Flux balancing the input photospheric flux map.
3. Reducing the maximum spherical harmonic l used in the computation from 180 to 120.
4. Decreasing model resolution from 1° to 2° (with concurrent decrease in maximum spherical harmonic l from 180 to 90).
5. Decreasing the source-surface height from 2.50 $R_\odot$ to 2.48 $R_\odot$
6. Modifying the field-line tracing step sizes from 0.010 and 0.050 $R_\odot$ (PFSS shell and SCS shell) to 0.012 and 0.052 $R_\odot$
7. Adding noise to the input maps.

These variations are intentionally minimal—the selected parameter values are all equally reasonable choices for a typical

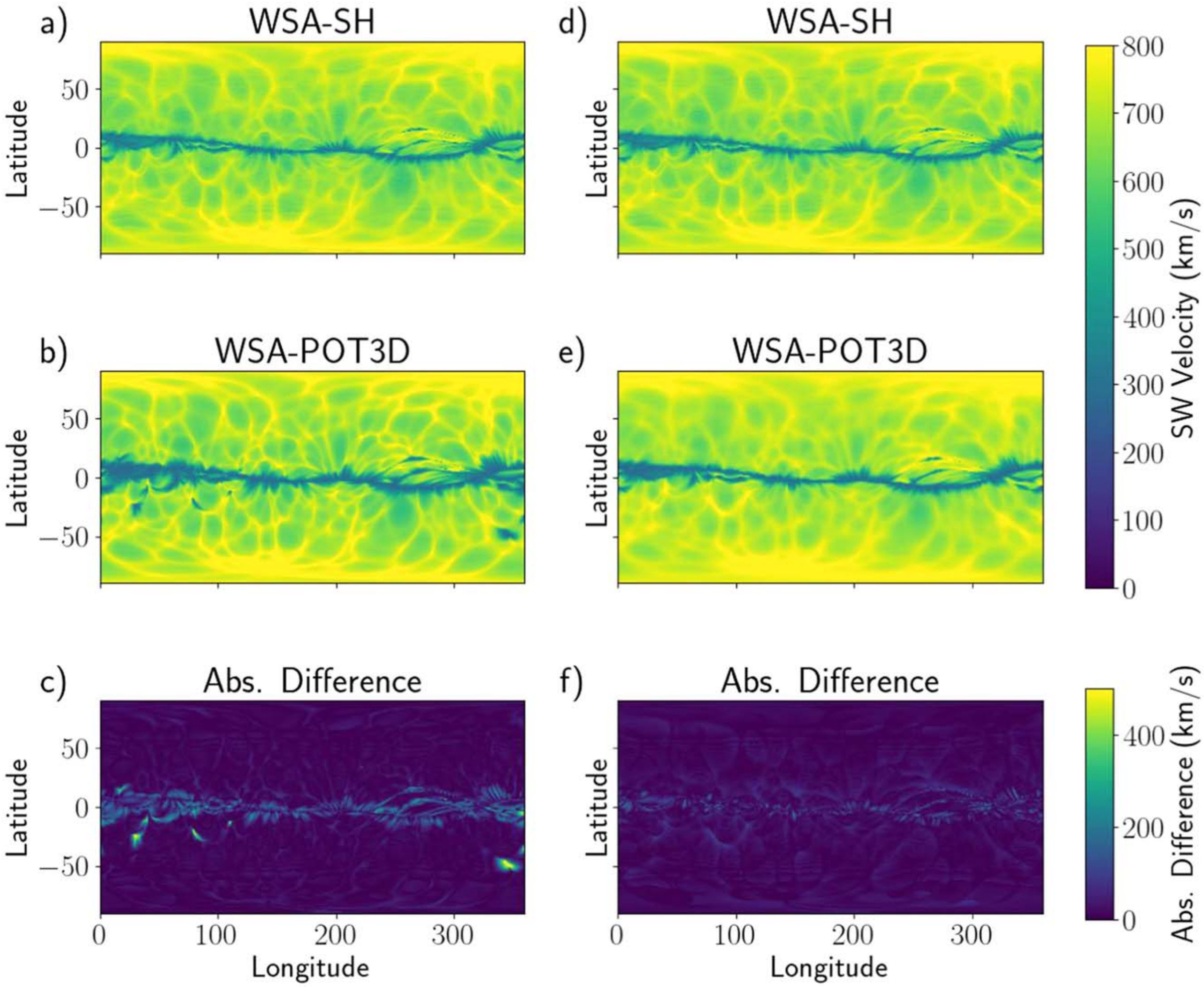

Figure 8. Model velocity prediction comparisons comparable to the one found in Figure 2 but where the open-flux locations have been determined by tracing the magnetic field from 1.01 $R_\odot$ rather than the photosphere, for the WSA-SH model only (left) and for both models (right).

WSA-SH use case, and the resulting set of models is intended to represent a minimal uncertainty in the WSA-SH calculation.

We used four different measures to quantify the similarity of the two model results: the percentage of outer boundary pixels that disagree about the magnetic field polarity; the root-mean-square differences in the magnetic field magnitude and asymptotic velocity predictions; and the WSA Prediction Metric (WPM), a joint measure of the accuracy of magnetic field polarity and solar wind speed predictions (Meadors et al. 2020). The WPM is designed for comparing time series of in situ measurements with WSA forecasts. Here, rather than compare time series at a single point in the heliosphere, we compare the predicted field polarity and terminal solar wind speed over the two models' outer boundaries:

$$\mathrm{WPM}(\mathrm{model}_1,\ \mathrm{model}_2) = \frac{\sigma_v}{0.5}\frac{\overline{|\Delta P(\theta,\ \phi)|}}{\sqrt{\overline{\Delta v(\theta,\ \phi)^2}}}, \tag{4}$$

where $\overline{\Delta P}$ and $\overline{\Delta v}$ are the area-weighted mean difference in the model-predicted IMF polarity and solar wind velocity of the two models, over the models' outer boundaries. The quantity σ_v is the square root of the area-weighted variance of the predicted solar wind speed over the WSA-SH velocity map in Figure 2 and is divided by 0.5 to account for the expected value of $\overline{\Delta P}$ for randomly chosen polarity predictions. The values of the four measures of agreement for these comparisons are given in Table 2 for the WSA-SH versus WSA-SH comparisons and the WSA-POT3D versus WSA-SH comparison.

For the first test shown in Table 2 (Mean ADAPT Ens. Comp.), we created WSA-SH models based on every member of the ADAPT ensemble, calculated the described model versus model measures of agreement (percent of polarity disagreement, $\Delta|B|_{\mathrm{RMS}}$, ΔV_{RMS}, and WPM) for all unique model pairings l and m, and then calculated the average value of each measure. For the final test ("Added noise to input maps"), we created 14 new versions of each member of the ADAPT ensemble. For each realization, we took bottom decile (lowest one-tenth of the flux values), calculated their standard deviation, and then added normally distributed noise with a standard deviation one quarter of that to the entire map. We then created a WSA-SH model for each of the resulting 180 maps. Measures of agreement were calculated for all unique model pairings based on the same original ADAPT ensemble member, and the resulting statistics were averaged over all ensemble members.

The polarity agreement and root-mean-square field difference are quite good for all of the comparisons, with the largest

Table 2
Quantitative Comparisons between WSA Models

		Polarity Disagreement (%)	$\Delta\lvert B\rvert_{\rm RMS}$	$\Delta V_{\rm RMS}$	WPM
WSA-SH versus WSA-SH (pert.)	Mean ADAPT Ens. Comp.	0.57	23.64	57.13	3.02
	Flux Balanced	0.07	8.070	16.27	10.91
	# SH Used (180 versus 120)	0.00	0.000	10.82	16.44
	Resolution (1° versus 2°)	0.19	11.601	43.84	3.94
	$R_{\rm SS}$ Height (2.48 versus 2.5 $R_\odot$)	0.01	3.489	20.06	8.87
	Field-tracing Step Size	0.00	0.000	16.56	10.75
	Added noise to input maps	0.01	3.414	27.43	7.35
WSA-POT3D versus WSA-SH		0.01	1.304	31.7	3.63

Note. The top section describes variations between the WSA-SH models under typical and *slightly* perturbed conditions, and the bottom result compares WSA-POT3D and WSA-SH models. Note that for the first three metrics, a lower value is better, while the opposite is true for the WPM.

disagreements being among the ADAPT ensemble members and between the 1° and 2° resolution models—both results not unexpected given the likelihood of shifting the location of the magnetic neutral line.

We might also have expected the change to the source-surface height to have a larger effect. However, the change we made here was very slight, and this particular model had a remarkably flat neutral line. Since changes in source-surface height tend to amplify (lower $R_{\rm ss}$) or deamplify (higher $R_{\rm ss}$) curvature in the magnetic neutral line, the relative lack of curvature may have mitigated the effect of the perturbation to $R_{\rm ss}$.

In general, the root-mean-square velocity differences were on the order of tens of kilometers per second, with the greatest variation being among the different ADAPT ensemble members. The velocity difference between the WSA-SH and WSA-POT3D models was comparable to the difference caused by changing the resolution of the model or adding random noise to the input maps but 2–3 times greater than the differences caused by changing the model parameters.

All four similarity measures indicate the greatest source of model uncertainty stems from the uncertainty in the input map, as exemplified in the ADAPT ensemble comparisons. This is despite the fact that the ensemble takes into account only the uncertainty about the supergranulation pattern, ignoring missing polar observations or flux emergence on the far side of the Sun.

5. Conclusions

We have presented a comprehensive comparison between WSA model solutions computed with the WSA-SH model based on a traditional spherical harmonic expansion and the finite-difference based WSA-POT3D model used in the CORHEL software suite. While the two codes solve the same potential field equation and the solutions are very similar, they are not completely identical. In particular, we explored differences in the locations of open-field regions and in the magnetic field and terminal solar wind speed at the outer boundary of the model, which is popular for use as an inner boundary condition for heliospheric models.

We have investigated the reasons for small differences between the models. The main difference in the magnetic field at the models' outer boundaries is in the polarities along the magnetic neutral line, where field lines from the two models trace to opposite poles. The differences in magnitude are small and typically of order 1%. The observed differences in the terminal solar wind speed appear not to result from substantial differences in the footpoint locations of the traced model field lines. They coincide primarily with locations where the velocity prediction equation is highly sensitive to small changes in the coronal hole boundary distance, Θ_B. Some areas, particularly in the midlatitudes of the southern hemisphere, showed differences due to the presence of small patches of closed magnetic field enclosed within the polar open-field region, which were present in one model but not the other.

The intercomparison of the finite-difference and spherical harmonic solutions lead to some interesting insights.

First, very slight differences in the model inputs or calculation lead to some very substantial differences in highly localized regions of the outer boundary. This presents a challenge for using in situ measurements for model assessment/comparison because it implies that forecast values for a particular location in the heliosphere can vary substantially due to only very small differences in the model parameters/inputs. When making these comparisons, it will be important to take into account which differences result from substantive inaccuracy of the model and which from chance in a region of high uncertainty.

Second, as higher-resolution input maps are more commonly used, greater complexity will be introduced in regions that were once largely unipolar. In the future, it will be necessary to come to terms with the impact of closed-flux regions within the boundaries of otherwise open regions on the asymptotic wind speeds produced using Equation (1) and to determine whether the resulting increased complexity in the predicted asymptotic wind speed is reliably predictive of heliospheric conditions.

Finally, the observed differences between the WSA-SH and WSA-POT3D models tend to be localized to very specific regions and generally smaller than, or of the same order as, the differences that can be found from reasonable variations in model inputs and/or parameters. In this sense, they represent a fundamental uncertainty in the values derived from the WSA model, illustrating that forecasts for space-weather conditions should be produced in ensembles that explicate this uncertainty.

Overall, the two model results are remarkably similar, but the highly sensitive nature of the WSA empirical relationship and differences in the arrangement of small patches of closed field in otherwise open-field regions, resulting from the spherical harmonic approximation used in the WSA-SH model, can produce important changes in the resulting solar wind velocity and IMF polarity predictions.

Acknowledgments

The authors wish to thank the anonymous referee for the thorough review of this paper. This work was supported by the

NSF/NASA SWQU program (grants AGS 2028154 and 80NSSC20K1582), the NASA LWS Strategic Capabilities Program (grant 80NSSC22K0893), and the NASA HGI program (grant 80NSSC19K0273). The ADAPT model development is supported by Air Force Research Laboratory (AFRL), along with AFOSR (Air Force Office of Scientific Research) tasks 18RVCOR126 and 22RVCOR012. The views expressed are those of the authors and do not reflect the official guidance or position of the United States Government, the Department of Defense (DoD) or of the United States Air Force. S.I.J. and C.N.A. are also partially supported by the NASA competed Heliophysics Internal Scientist Funding Model (ISFM).

ORCID iDs

Shaela I. Jones https://orcid.org/0000-0001-9498-460X
Ronald M. Caplan https://orcid.org/0000-0002-2633-4290
C. Nick Arge https://orcid.org/0000-0001-9326-3448
Jon A. Linker https://orcid.org/0000-0003-1662-3328
Carl J. Henney https://orcid.org/0000-0002-6038-6369
Raphael Attie https://orcid.org/0000-0003-4312-6298
Cooper Downs https://orcid.org/0000-0003-1759-4354
Bibhuti Kumar Jha https://orcid.org/0000-0003-3191-4625
James Turtle https://orcid.org/0000-0003-0735-7769
Lisa Upton https://orcid.org/0000-0003-0621-4803

References

Altschuler, M. D., & Newkirk, G. 1969, SoPh, 9, 131
Arge, C. N., Henney, C. J., Hernandez, I. G., et al. 2013, in AIP Conf. Proc. 1539, Solar Wind 13: Proc. of the Thirteenth Int. Solar Wind Conf., ed. G. P. Zank et al. (Melville, NY: AIP), 11
Arge, C. N., Henney, C. J., Koller, J., et al. 2010, in AIP Conf. Proc. 1216, Twelfth Int. Solar Wind Conf., ed. Milan Maksimovic (Melville, NY: AIP), 343
Arge, C. N., Luhmann, J. G., Odstrcil, D., Schrijver, C. J., & Li, Y. 2004, JASTP, 66, 1295
Arge, C. N., Odstrcil, D., Pizzo, V. J., & Mayer, L. R. 2003, in AIP Conf. Proc. 679, Solar Wind Ten: Proc. of the Tenth Int. Solar Wind Conf., ed. M. Velli et al. (Melville, NY: AIP), 190
Arge, C. N., & Pizzo, V. J. 2000, JGR, 105, 10465
Barnes, G., DeRosa, M. L., Jones, S. I., et al. 2023, ApJ, 946, 105
Caplan, R. M., Downs, C., Linker, J., & Mikic, Z. 2021a, POT3D, v3.1.0r1, Zenodo, doi:10.5281/zenodo.4690005
Caplan, R. M., Downs, C., Linker, J. A., & Mikic, Z. 2021b, ApJ, 915, 44
Henney, C. J. 2020, adapt40411_03l012_202002022000_i00030000n1.fts.gz, v3.1220, Zenodo, doi:10.5281/zenodo.8216027
Hickmann, K. S., Godinez, H. C., Henney, C. J., & Arge, C. N. 2015, SoPh, 290, 1105
Kim, T. K., Pogorelov, N. V., Arge, C. N., et al. 2020, ApJS, 246, 40
Levine, R. H., Altschuler, M. D., & Harvey, J. W. 1977, JGR, 82, 1061
Linker, J. A., Riley, P., Mikic, Z., et al. 2009, AGUFM, 2009, SA43A–1612
Mathews, J. H., & Fink, K. K. 2004, Numerical Methods Using Matlab (4th ed.; Englewood Cliffs, NJ: Prentice-Hall)
McGregor, S. L., Hughes, W. J., Arge, C. N., Owens, M. J., & Odstrcil, D. 2011, JGRA, 116, A03101
Meadors, G. D., Jones, S. I., Hickmann, K. S., et al. 2020, SpWea, 18, e02464
Odstrcil, D., Pizzo, V. J., & Arge, C. N. 2005, JGRA, 110, A02106
Pahud, D. M., Merkin, V. G., Arge, C. N., Hughes, W. J., & McGregor, S. M. 2012, JASTP, 83, 32
Schatten, K. H., Wilcox, J. M., & Ness, N. F. 1969, SoPh, 6, 442
Schonfeld, S. J., Henney, C. J., Jones, S. I., & Arge, C. N. 2022, ApJ, 932, 115
Schou, J., Scherrer, P. H., Bush, R. I., et al. 2012, SoPh, 275, 229
Sheeley, N. R. J. 2017, HGSS, 8, 21
Tóth, G., van der Holst, B., & Huang, Z. 2011, ApJ, 732, 102
Wallace, S., Arge, C. N., Viall, N., & Pihlström, Y. 2020, ApJ, 898, 78
Wang, Y. M., & Sheeley, N. R. J. 1990, ApJ, 355, 726
Wang, Y. M., & Sheeley, N. R. J. 1995, ApJL, 447, L143
Wang, Y.-M., Sheeley, N., Arge, C. N., et al., 2022 WSA_CAT, v5.3.4, NASA SMCE Gitlab